

Supporting Information

Vapor-Fed Photoelectrolysis of Water at 0.3 V Using Gas-Diffusion Photoanodes of SrTiO₃ Layers

Fumiaki Amano,^{ab} Hyosuke Mukohara,^a Hiroki Sato,^a Chihiro Tateishi,^a Hiromasa Sato,^c
and Toshiki Sugimoto^{bc}*

^a Department of Chemical and Environmental Engineering, The University of Kitakyushu, 1-1 Hibikino, Wakamatsu, Kitakyushu, Fukuoka 808-0135, Japan.

^b Precursory Research for Embryonic Science and Technology (PRESTO), Japan Science and Technology Agency (JST), 4-1-8 Honcho, Kawaguchi, Saitama 332-0012, Japan.

^c Department of Materials Molecular Science, Institute for Molecular Science, Okazaki, Aichi 444-8585, Japan

Corresponding Author

*Fumiaki Amano, E-mail: amano@kitakyu-u.ac.jp

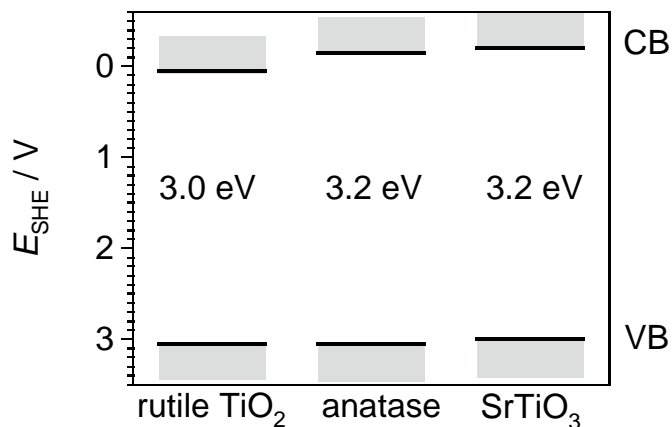


Figure S1. Band diagram of rutile TiO_2 , anatase TiO_2 , and SrTiO_3 . The reported flat band potential is used for the conduction band (CB) minimum. Valence band (VB) maximum is determined from the band gap energy.

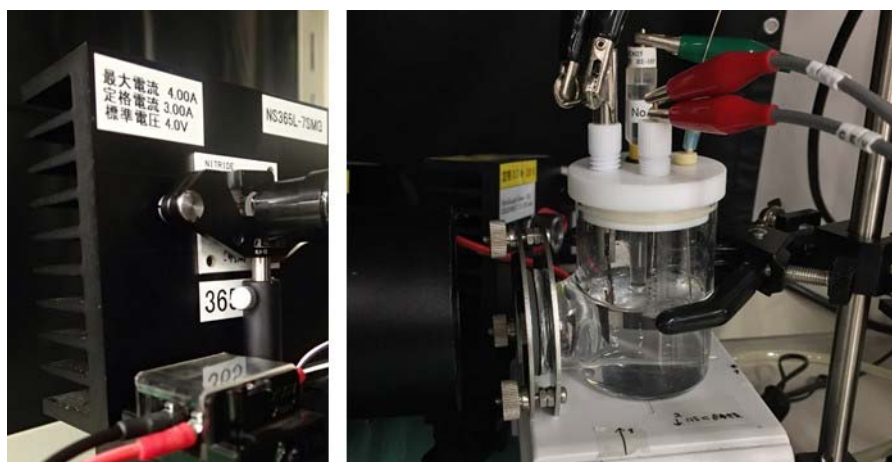


Figure S2. Experimental setup of photoelectrochemical (PEC) measurement in aqueous electrolyte. One-compartment glass reactor was used for three electrode system consisting of an Ag/AgCl reference electrode and a platinum wire counter electrode.

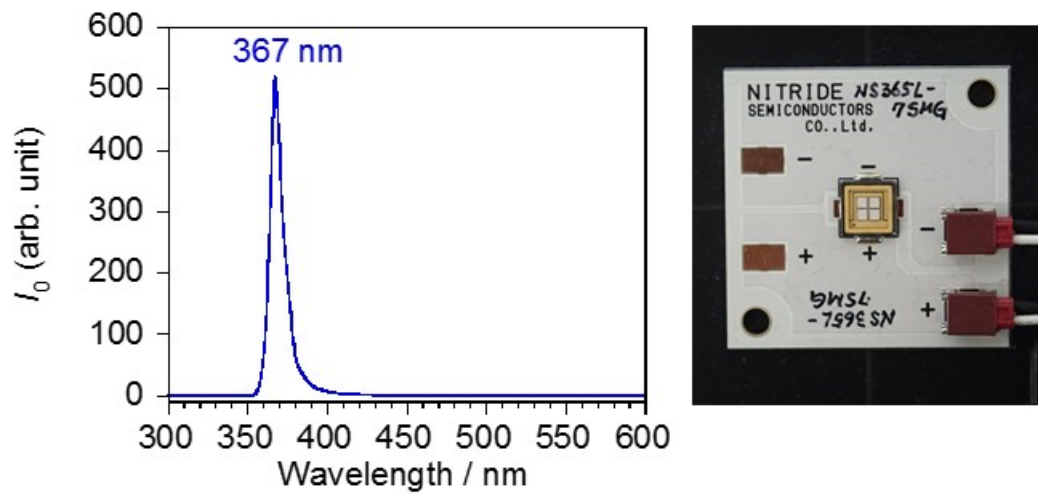


Figure S3. Emission spectrum of 365-nm UV LED for the PEC measurement. The peak wavelength was 367 nm. The half width at half maximum was about 10 nm.

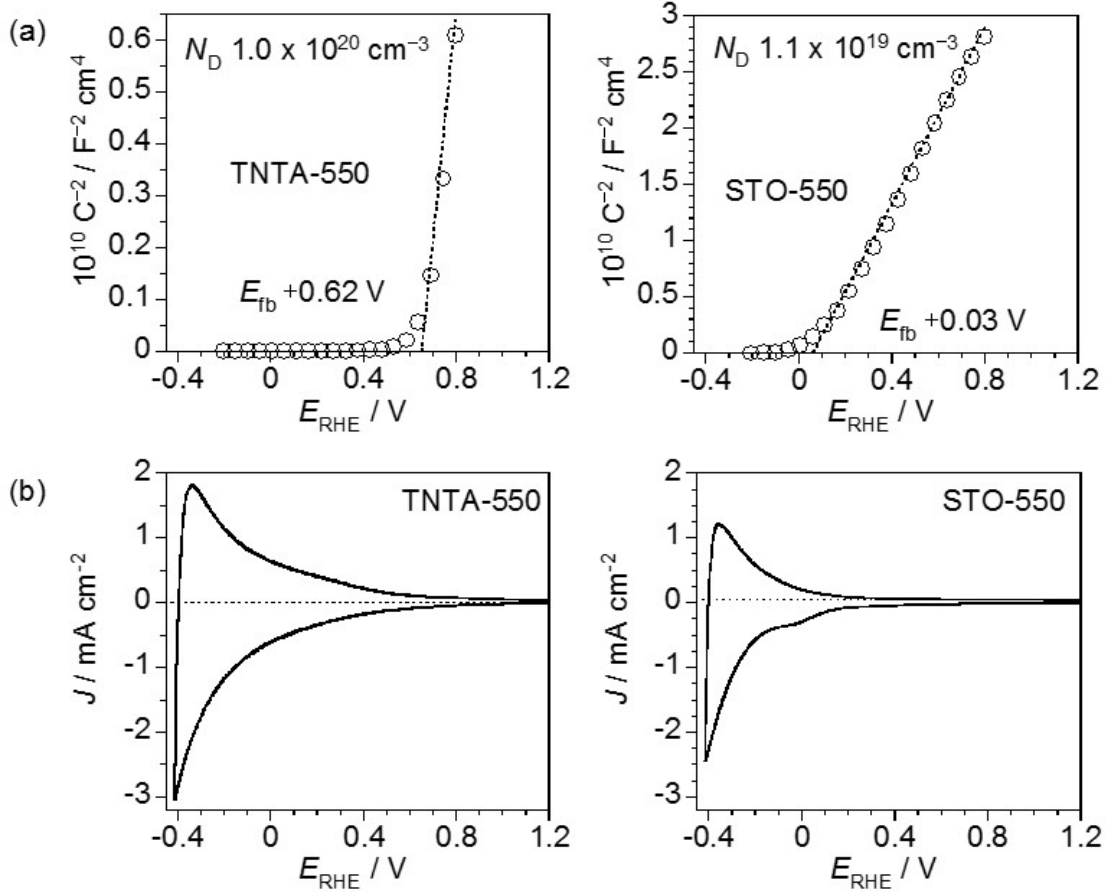


Figure S4. (a) Mott-Schottky plots and (b) cyclic voltammograms of TNTA-550 and STO-550 in an aqueous electrolyte (pH = 6.7). The space charge layer capacitance (C) was measured by a VersaSTAT 4 potentiostat with a frequency response analyser (Ametek, USA) using electrochemical impedance method at a frequency of 1000 Hz. Flatband potential (E_{FB}) was determined by using the Mott-Schottky equation, $1/C^2 = (2/(q \epsilon \epsilon_0 N_D)) (E - E_{fb} - kT/q)$, where q is the elementary electric charge, ϵ is the dielectric constant, ϵ_0 is the permittivity of the vacuum and kT/q is the thermal voltage. The donor density (N_D) of the n-type semiconductor was calculated from the positive slope using $\epsilon = 31$ for anatase TiO_2 and $\epsilon = 332$ for rutile SrTiO_3 .

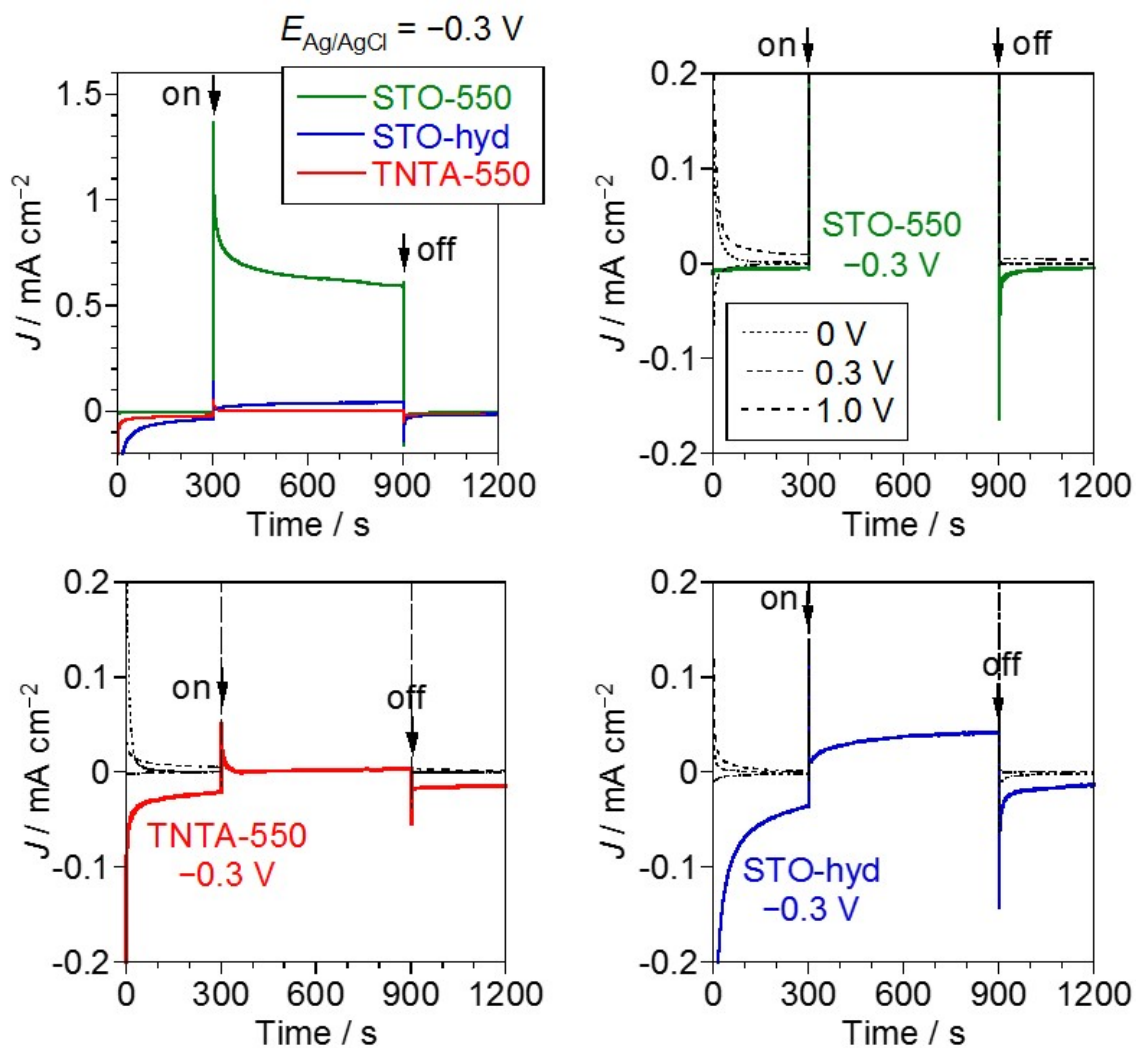


Figure S5. Current density (J)-time curves of TNTA-550, STO-hyd, and STO-550 in an aqueous solution of Na_2SO_4 and phosphate buffer (pH 6.7) at $E_{\text{Ag}/\text{AgCl}} = -0.3 \text{ V}$ under 365-nm UV (43 mW cm^{-2}). The dashed curves show the photocurrent responses obtained at $E_{\text{Ag}/\text{AgCl}} = 0 \text{ V}$, 0.3 V , and 1.0 V . The cathodic J was observed for TNTA-550 and STO-hyd at $E_{\text{Ag}/\text{AgCl}} = -0.3 \text{ V}$ in the absence of UV irradiation.

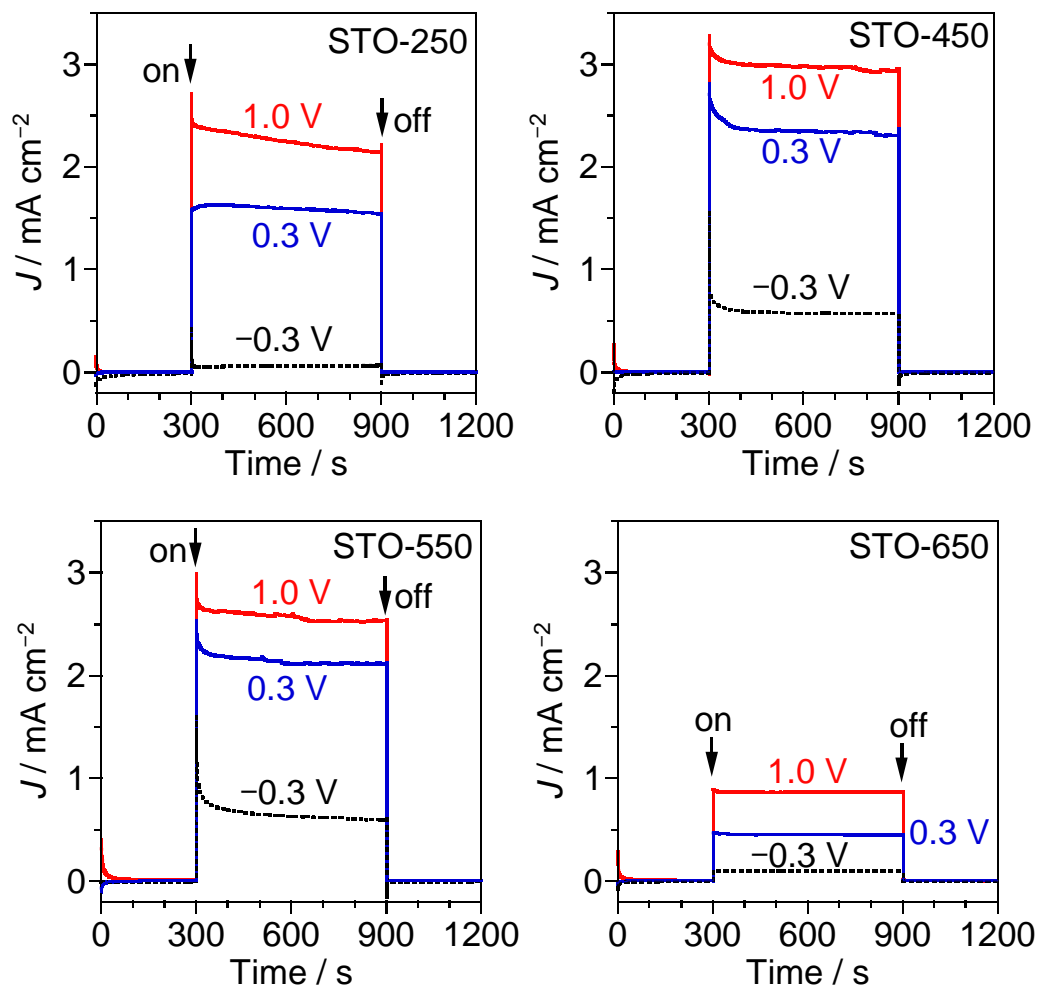


Figure S6. Current density (J)-time curves of STO-250, STO-450, STO-550, and STO-650 in an aqueous solution of Na_2SO_4 and phosphate buffer (pH 6.7) at different applied potentials ($E_{\text{Ag}/\text{AgCl}} = -0.3 \text{ V}$, 0.3 V , and 1.0 V) under 365-nm UV (43 mW cm^{-2}). The sample prepared by calcination of STO-hyd at $x \text{ }^\circ\text{C}$ is denoted as STO- x .

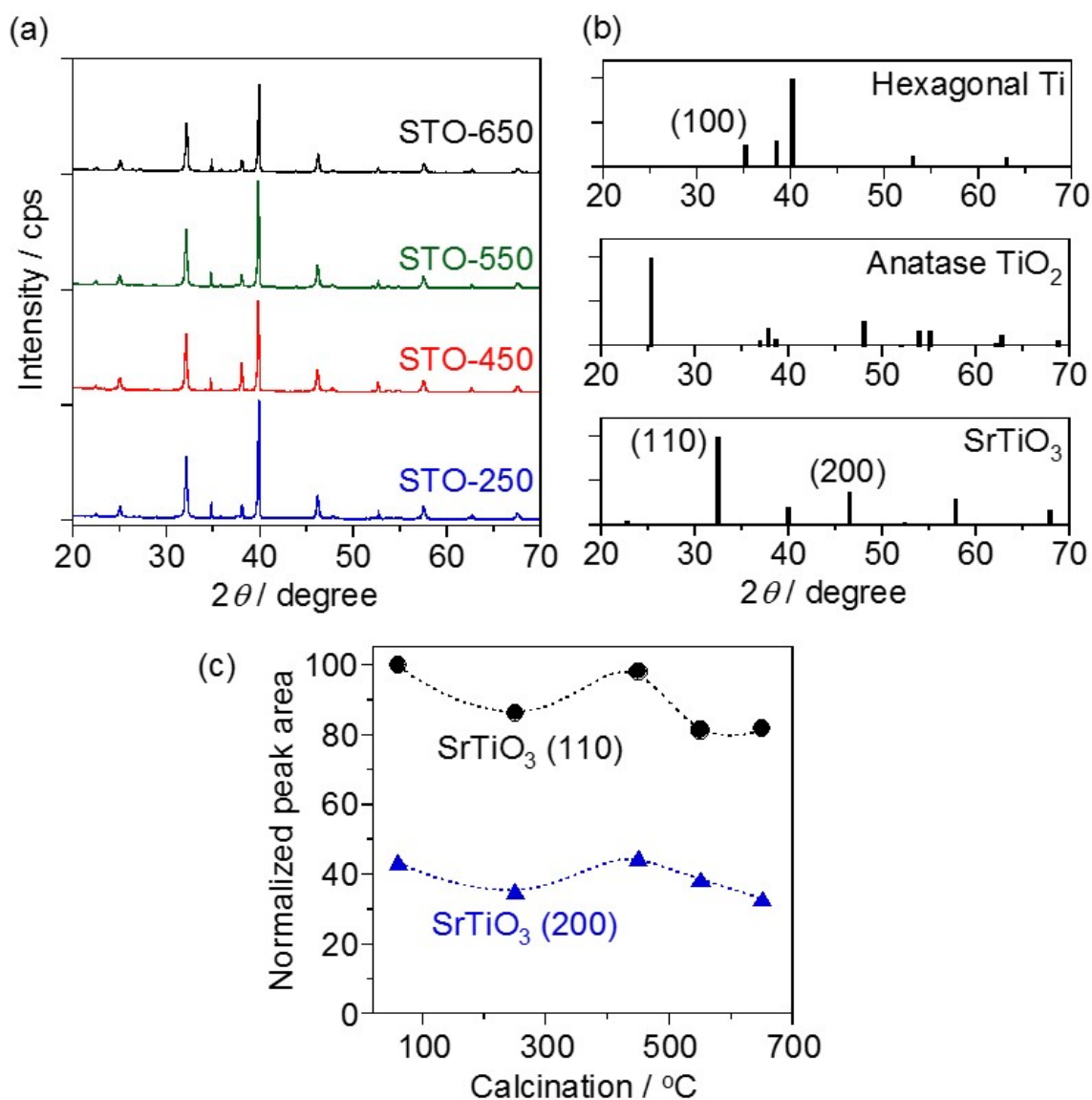


Figure S7. (a) XRD patterns of STO-250, STO-450, STO-550, and STO-650, which were translated in the y-axis direction for clarity. (b) Powder diffraction file (PDF) provided by the international centre for diffraction data (ICDD): hexagonal α -Ti (PDF 00-044-1294), anatase TiO₂ (PDF 00-021-1272), and SrTiO₃ (PDF 01-070-8508). (c) Peak area of SrTiO₃ (110) and (200) normalized to the peak area of hexagonal Ti (100) as a function of calcination temperature.

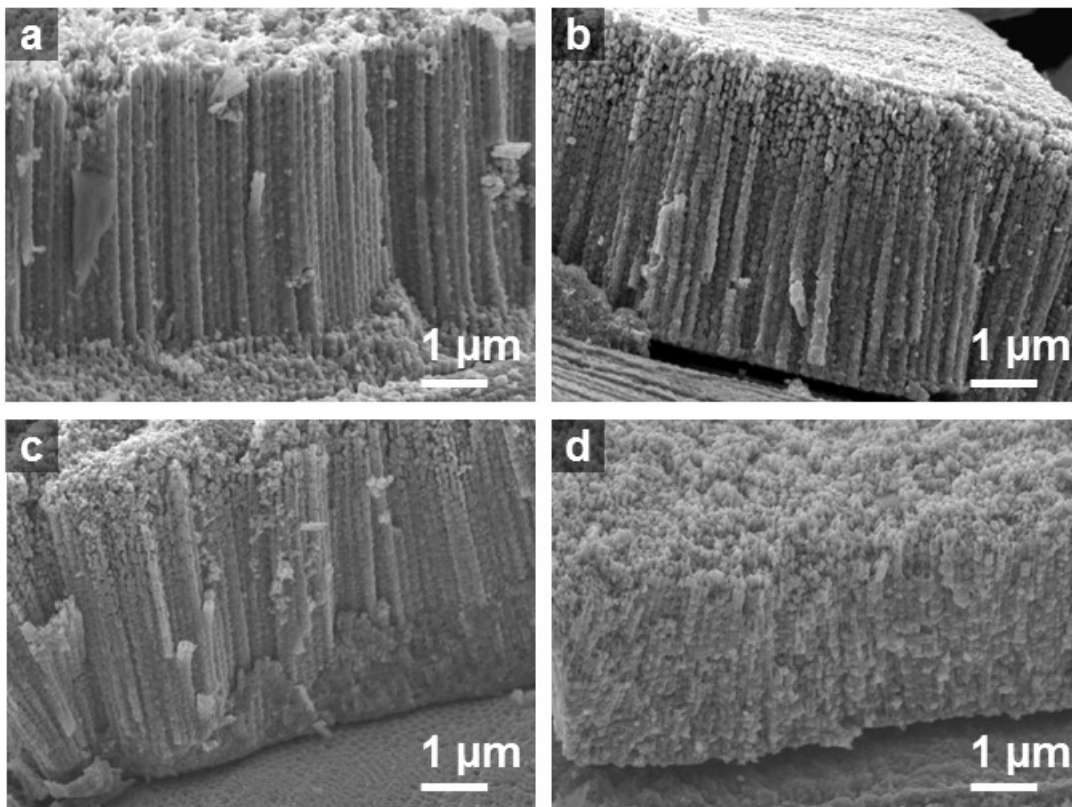


Figure S8. SEM images of the cross-sectional side view of the SrTiO₃ layer decorated on the Ti microfiber: (a) STO-250, (b) STO-450, (c) STO-550, and (d) STO-650.

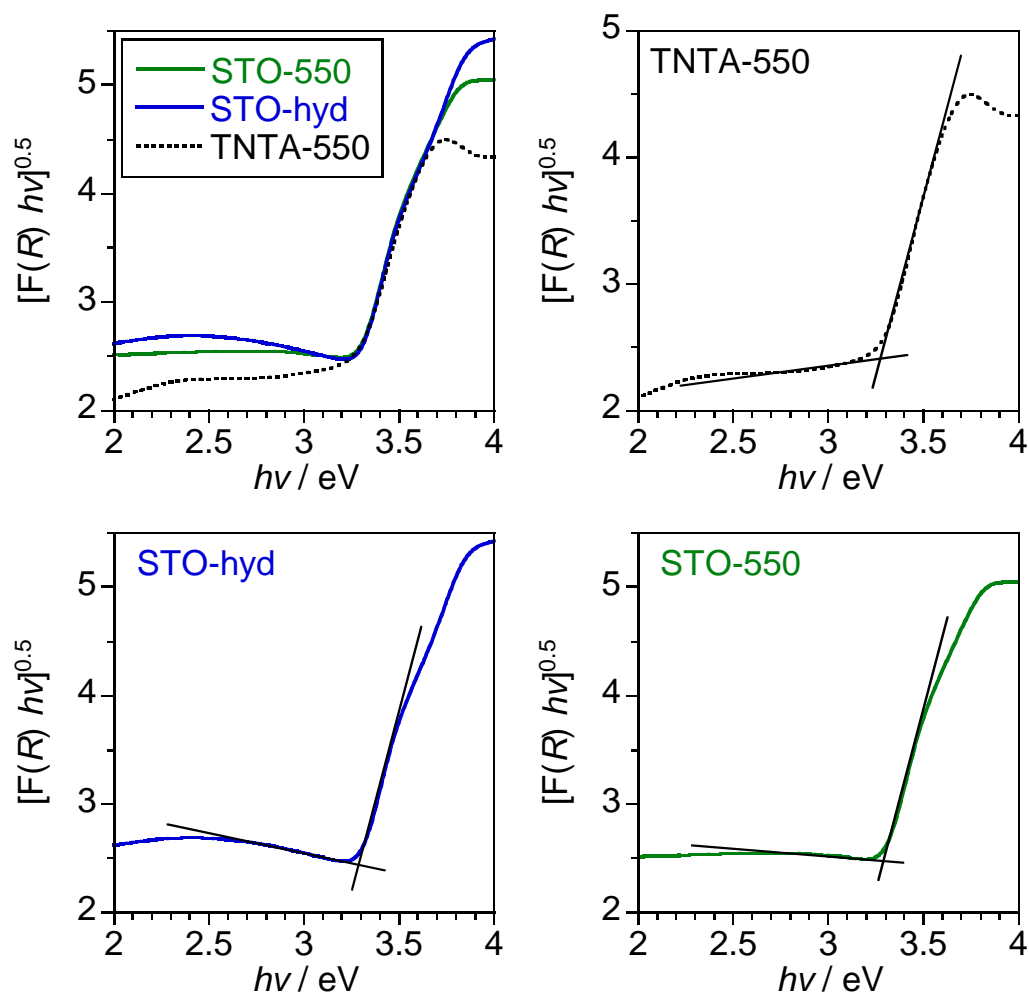


Figure S9. Tauc plots of TNTA-550, STO-hyd, and STO-550. The band-gap energy (E_g) was obtained by the intersection between the baseline and the straight line near the absorption edge in the plot of $(F(R) hv)^{0.5}$ against hv . The $F(R)$ is the Kubelka–Munk function, $F(R) = (1-R)^2 / (2R)$, where R is the relative reflectance measured in diffuse reflectance UV-vis spectroscopy. The indirect E_g was found to be 3.24, 3.26, and 3.25 eV for TNTA-550, STO-hyd, and STO-550, respectively



Figure S10. Photos of a membrane electrode assembly. The left-side photograph shows the side of the ionomer-coated oxide layers on the titanium microfiber felt. The right-side photograph shows the side of the ionomer-mixed Pt/CB film as an H₂-evolving cathode.

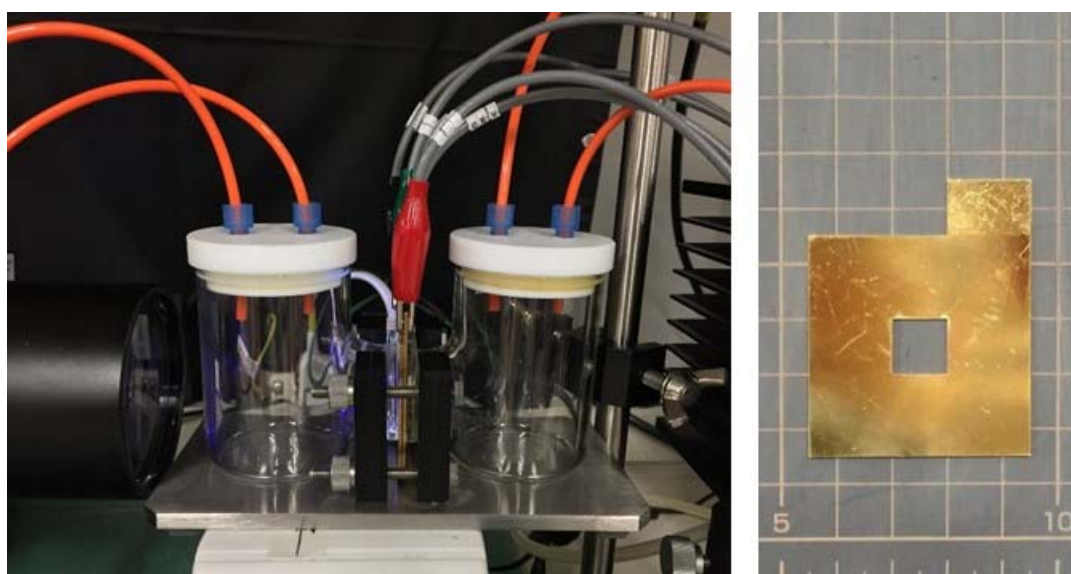


Figure S11. Photos of an H-type dual-compartment glass reactor for gas-phase PEC reaction and a gold-coated copper plate with a square window for UV (irradiation area 1×1 cm²).

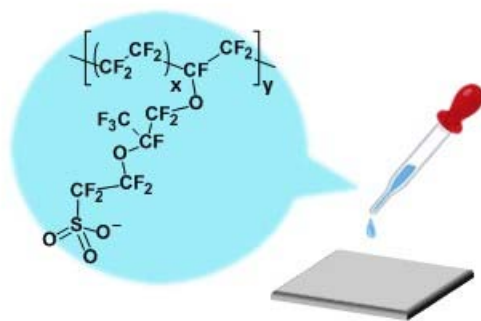
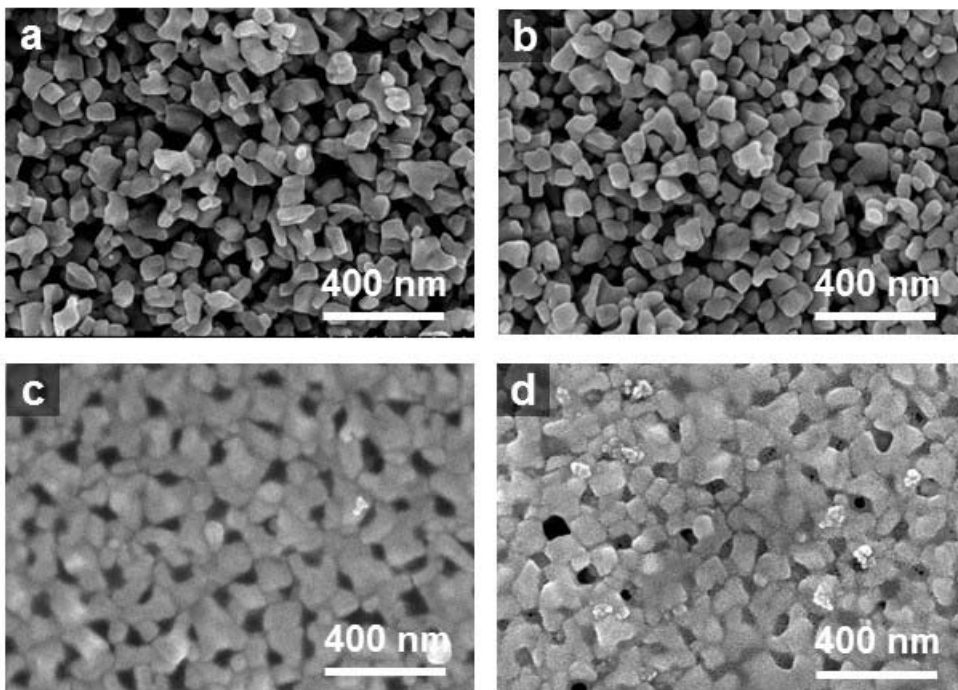


Figure S12. SEM images of the surface of (a) bare STO-550, (b) bare STO-550 after gold sputtering, (c) the Nafion ionomer-coated STO-550, and (d) the Nafion ionomer-coated STO-550 after gold sputtering. The Nafion ionomer-coated STO-550 was dried at 80 °C after the drop cast of the ionomer dispersion.

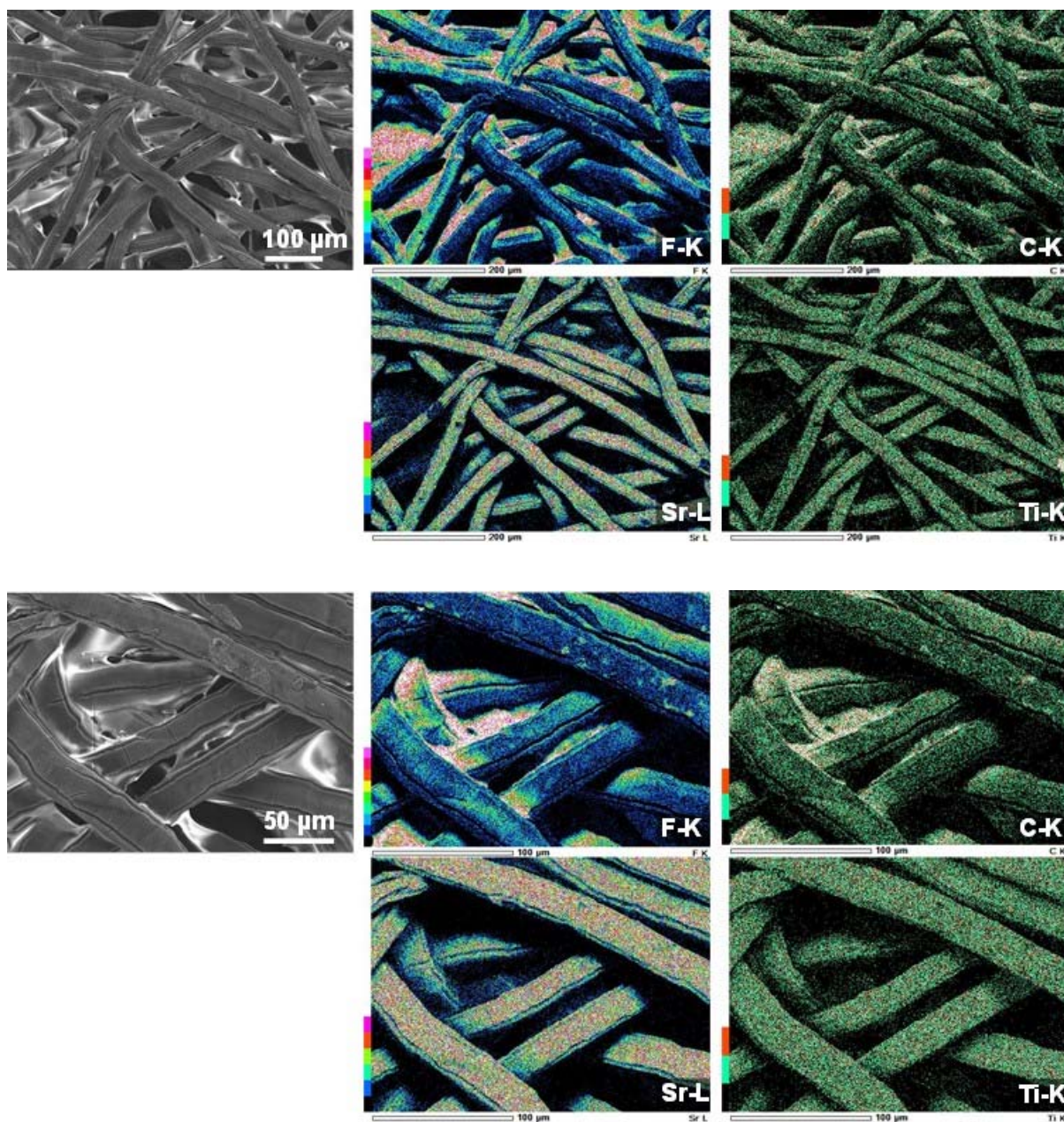


Figure S13. SEM images and EDS elemental (fluorine, carbon, strontium, and titanium) mapping images of STO-550. The upper and bottom images are observed in magnification of $\times 200$ and $\times 500$. The element concentration is indicated by the colour bar located at the left bottom of each map. Higher concentrations are red to white, whereas lower concentrations are blue to black.

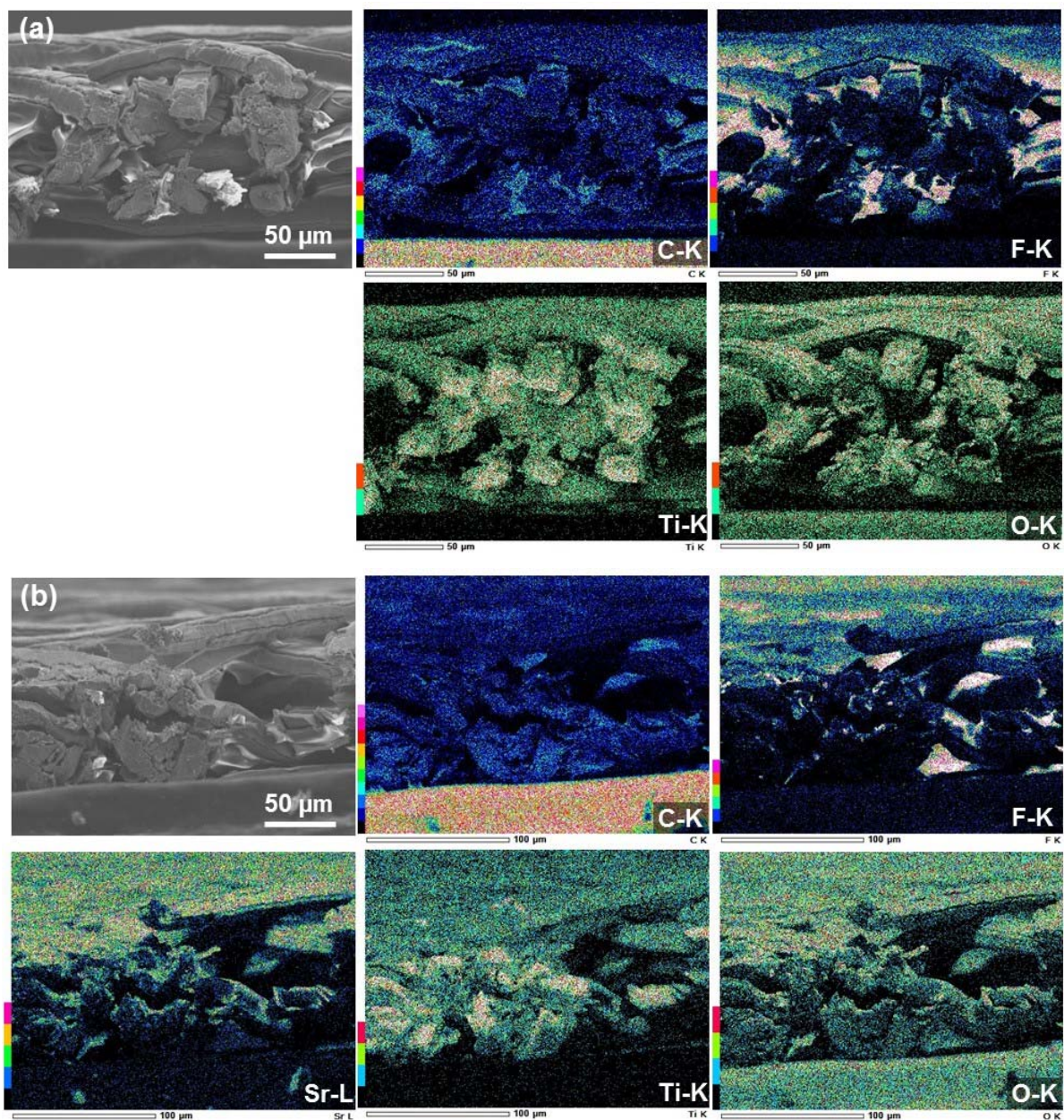


Figure S14. SEM image and EDS elemental (carbon, fluorine, strontium, titanium, and oxygen) mappings for the cross-section of the (a) TNTA-550 and (b) STO-550 microfiber felts with four coats of Nafion ionomer. The element concentration is indicated by the colour bar located at the left bottom of each map. Higher concentrations are red to white, whereas lower concentrations are blue to black.



Figure S15. A photo of a planar-type dual-compartment stainless-steel reactor with irradiation area of 2.0 cm^2 ($1.4 \times 1.4 \text{ cm}^2$).

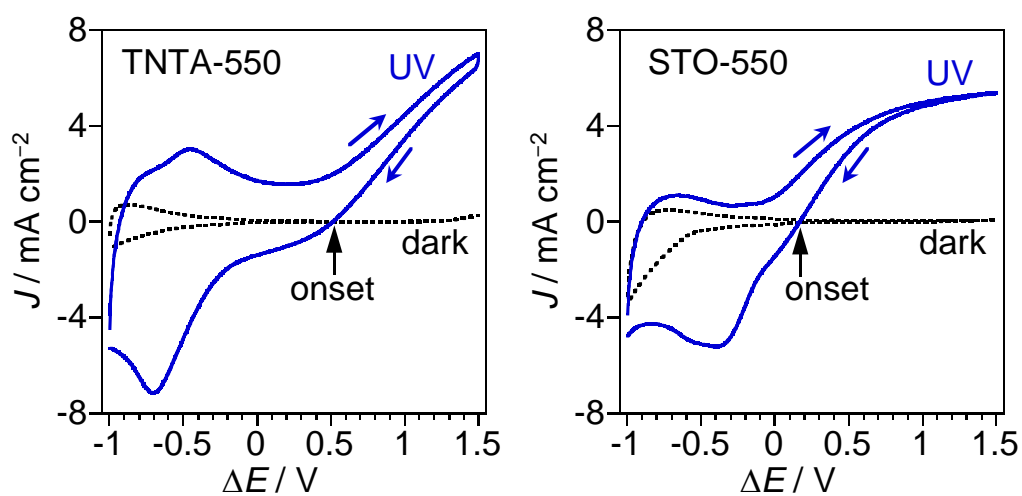


Figure S16. Cyclic voltammograms of the ionomer-coated photoanode (TNTA-550 and STO-550) in humidified argon (3 vol% water vapor) and under 365-nm UV ($I_0 = 42 \text{ mW cm}^{-2}$, irradiation area 2 cm^2).

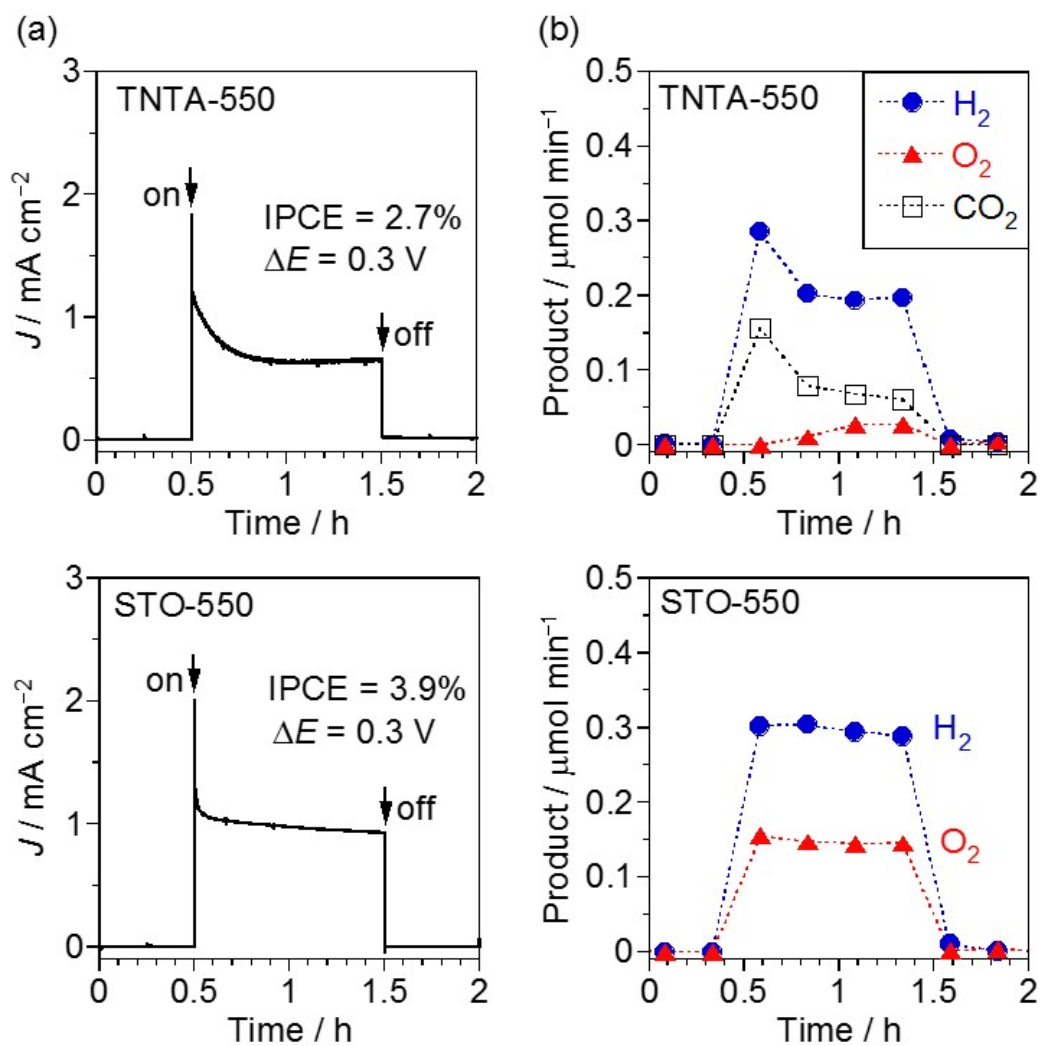


Figure S17. PEC water vapor splitting by ionomer-coated photoanode | PEM | Pt/CB under 365-nm UV ($I_0 = 42 \text{ mW cm}^{-2}$, area 2 cm^2) at $\Delta E = 0.3$ V. The data are enlargement of the data shown in Figure 9. (a) Photocurrent response of the ionomer-coated photoanode (TNTA-550 and STO-550) in humidified argon (3 vol% water vapor). (b) The formation rate of H_2 in the cathode compartment and the O_2 and CO_2 in the photoanode compartment. For STO-550, CO_2 was not detected in this condition.

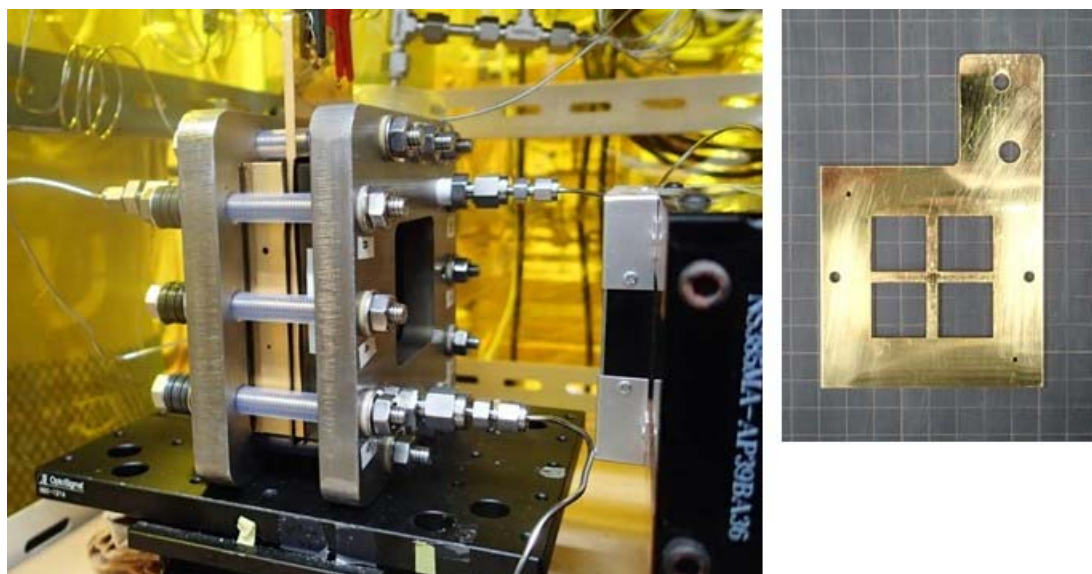


Figure S18. Photos of a planar-type dual-compartment stainless-steel reactor for gas-phase PEC reaction and a gold-coated copper plate with four square windows with UV irradiation area of 16.0 cm^2 (four $2 \times 2 \text{ cm}^2$).

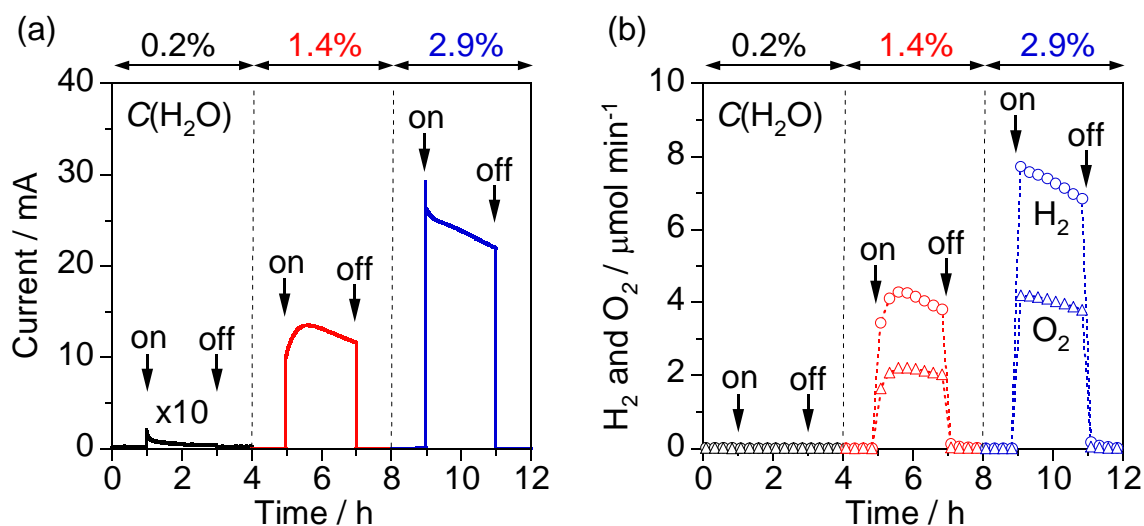


Figure S19. Effect of water vapor concentration, $C(\text{H}_2\text{O})$, on the PEC water vapor splitting by ionomer-coated STO-550 | PEM | Pt/CB under 365-nm UV ($I_0 = 40 \text{ mW cm}^{-2}$, area 16 cm^2) at $\Delta E = 1.2 \text{ V}$. (a) Photocurrent response. (b) H_2 and O_2 formation rate in the cathode and the photoanode compartment, respectively. The $C(\text{H}_2\text{O})$ of both compartments was changed from 0.2% to 1.4% and 2.9% at room temperature ($25 \text{ }^\circ\text{C}$) under atmospheric pressure (101 kPa).

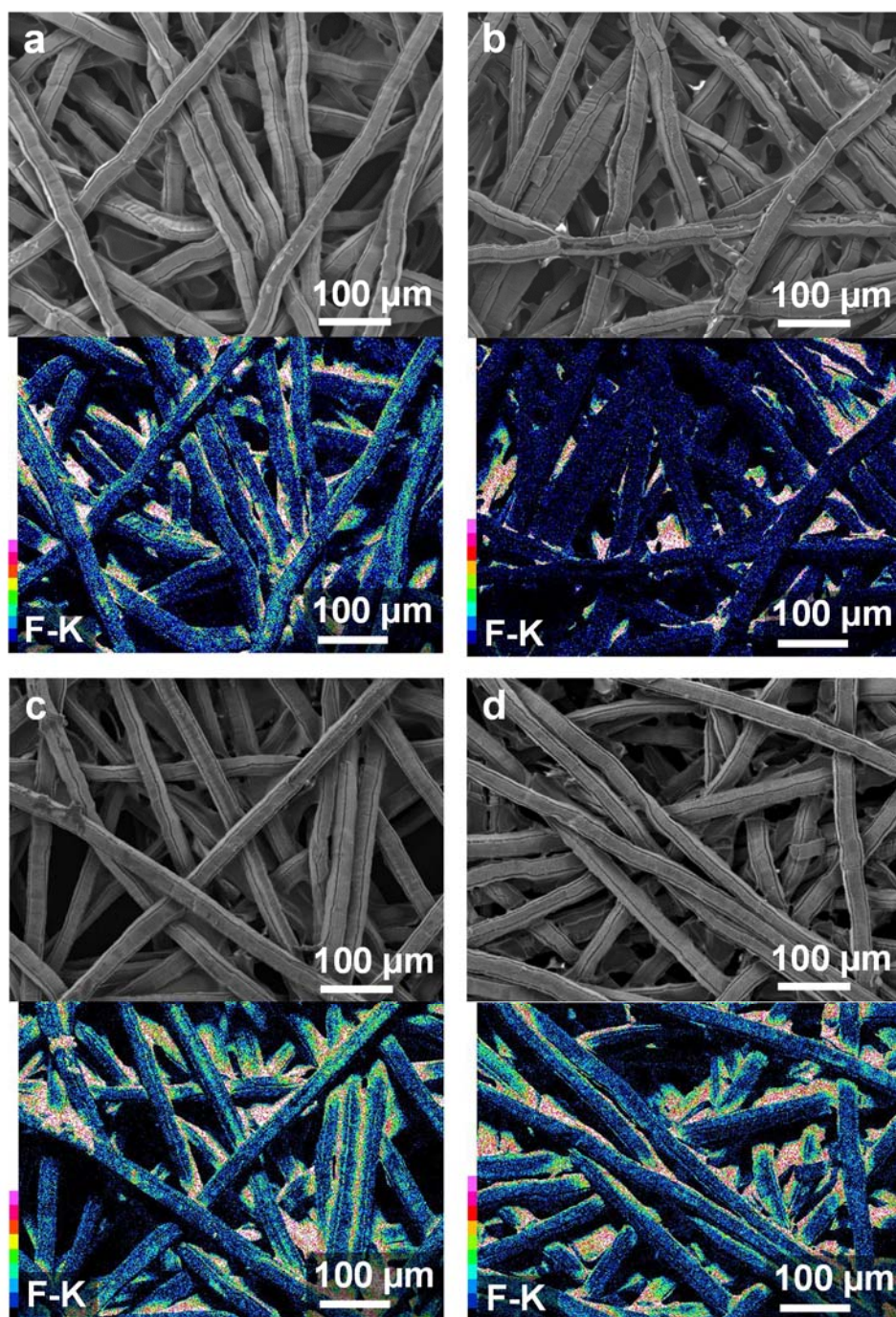


Figure S20. SEM images and EDS fluorine mapping images of (a, b) TNTA-550 and (c, d) STO-550. The (a, c) shows the images before the PEC reaction. The (b, d) shows the images after PEC water vapor splitting at 1.2 V under 365-nm UV ($I_0 = 40 \text{ mW cm}^{-2}$, area 16 cm^2) for 10 h.